Computers & Geosciences 85 (2015) 248–257

Contents lists available at ScienceDirect

Computers & Geosciences

journal homepage: www.elsevier.com/locate/cageo

Case study

Optical granulometric analysis of sedimentary deposits by color segmentation-based software: OPTGRAN-CS

G. Moreno Chávez [a,1], D. Sarocchi [b,*], E. Arce Santana [c], L. Borselli [b]

[a] Doctorado Institucional en Ingeniería y Ciencias de Materiales, c/o Instituto de Geología UASLP, Av. Dr. M. Nava No. 5, Zona Universitaria, 78290 San Luis Potosí, México
[b] Instituto de Geología/Facultad de Ingeniería UASLP, Av. Dr. M. Nava No. 5, Zona Universitaria, 78290 San Luis Potosí, México
[c] Facultad de Ciencias, UASLP, Diagonal Sur S/N, Zona Universitaria, 78290 San Luis Potosí, México

ARTICLE INFO

Article history:
Received 4 June 2015
Received in revised form
5 September 2015
Accepted 8 September 2015
Available online 12 September 2015

Keywords:
Optical granulometry
Image segmentation
Stereology

ABSTRACT

The study of grain size distribution is fundamental for understanding sedimentological environments. Through these analyses, clast erosion, transport and deposition processes can be interpreted and modeled. However, grain size distribution analysis can be difficult in some outcrops due to the number and complexity of the arrangement of clasts and matrix and their physical size. Despite various technological advances, it is almost impossible to get the full grain size distribution (blocks to sand grain size) with a single method or instrument of analysis. For this reason development in this area continues to be fundamental. In recent years, various methods of particle size analysis by automatic image processing have been developed, due to their potential advantages with respect to classical ones; speed and final detailed content of information (virtually for each analyzed particle). In this framework, we have developed a novel algorithm and software for grain size distribution analysis, based on color image segmentation using an entropy-controlled quadratic Markov measure field algorithm and the Rosiwal method for counting intersections between clast and linear transects in the images. We test the novel algorithm in different sedimentary deposit types from 14 varieties of sedimentological environments. The results of the new algorithm were compared with grain counts performed manually by the same Rosiwal methods applied by experts. The new algorithm has the same accuracy as a classical manual count process, but the application of this innovative methodology is much easier and dramatically less time-consuming. The final productivity of the new software for analysis of clasts deposits after recording field outcrop images can be increased significantly.

1. Introduction

One of the most important textural characteristics of a rock consisting of clasts or sediments is the size of the clasts that compose it; that is, their granulometric distribution and the degree of uniformity of clast sizes. The importance that geologists has always given to this textural feature is amply demonstrated by the enormous amount of literature on the subject (Boudon et al., 1993; Allen, 1997).

The size of the particles constituting a rock or a deposit is strongly related to their origin and affected by transport and deposition mechanisms. Detailed study of this property can therefore provide information of utmost importance for understanding the nature of the rock itself and the events that originated it (Folk, 1966; Glenn, 1969; Pettijohn, 1987; Allen, 1997; Nichols, 2009). However, to obtain the whole granulometric distribution of an outcrop is, in many cases, a complicated task. Sedimentary deposits are often characterized by a wide range of grain sizes, ranging from a few microns to several meters (Gee and Bauder, 1986; Lirer and Vinci, 1991; Valsangkar, 1992).

In many fields of sedimentology such as volcanic sedimentology, until the 1980s and also in recent times, most sedimentological studies were based only on granulometric data obtained by sieving (Walker, 1971; Yamazaki et al., 1973; Lajoie et al., 1989; Saucedo et al., 2002), with few exceptions (Freundt and Schmincke, 1986).

In more recent times the extreme granulometric classes of distributions have also been begun to be considered, and rightly so. Thin tails were analyzed using sedimentographic scanning (Lewis and Mcconchie, 1994; Konert and Vandenberghe, 1997; Beuselinck et al., 1998) or stream scanning (Allen, 1997, Kaye et al., 1999) methods, and the coarser tails were analyzed using image

* Corresponding author. Fax: +52 444 8111741.
E-mail addresses: gamalielmch@gmail.com (G.M. Chávez), sarocchi@gmail.com (D. Sarocchi), arce@fciencias.uaslp.mx (E.A. Santana), lborselli@gmail.com (L. Borselli).
[1] Fax: +52 444 8111741.

http://dx.doi.org/10.1016/j.cageo.2015.09.007
0098-3004/

analysis techniques (Capaccioni and Sarocchi, 1996, Capaccioni et al., 1997; Sahagian and Proussevitch, 1998; Sarocchi et al., 2005; Saucedo et al., 2008; Sarocchi et al., 2011). Complete and correct granulometry studies cannot be performed if parts of the distribution are missing.

Most granulometric methods used in sedimentology allow only part of the granulometric spectrum to be analyzed and, in many cases, it is necessary to combine the results provided by different methods to reconstruct the whole particle size distribution (Gee and Bauder, 1986; Lovell and Rose, 1991; Olgun and Norman, 1993; Loizeau et al., 1994; Konert and Vandenberghe, 1997; Sarocchi et al., 2011). However this implies having to gather information related to different physical properties of particles, making assumptions and simplifications.

The granulometric optical method (Capaccioni and Sarocchi, 1996; Capaccioni et al., 1997; Konert and Vandenberghe, 1997; Sarocchi et al., 2005, 2011) based on obtaining particle size data from a digital photograph and using stereological methods (Mouton, 2002) is one of the granulometric techniques that has excelled in recent years. The reasons for its success are: (1) the accuracy achievable by measuring a sufficiently large number of particles; and (2) the size range which can be analyzed. Practically it can be applied at any scale, simply by changing the optical device used for taking the pictures; and (3) it is a conservative approach that does not require a physical sample (Capaccioni and Sarocchi, 1996; Capaccioni et al., 1997; Fernlund, 1998; Chermant, 2001; Rubin, 2004; Sarocchi et al., 2011; Moreno Chávez et al., 2014).

Due to the difficulty in segmenting images of sedimentary outcrops in order to separate clasts from the matrix, the method has been used manually to date, resulting in an enormous waste of time (Sarocchi et al., 2011, Moreno Chávez et al., 2014). This complexity is due to the huge variety of sedimentary deposits, which have different colors, textures and shapes, as well as sedimentary structures, and potentially shadows, or mossy, vegetated or damp areas.

In order to solve the problem of segmentation in images of sedimentary deposits, in this paper we propose a new method of supervised automatic counting, based on segmentation for color image, using Entropy-Controlled Quadratic Markov Measure Field Models (ECQMMF) developed by Rivera and Dalmau (2012). OPTGRAN-CS software provides optical granulometry from an ECQMMF-based segmentation. The program, using the mask and Rosiwal's stereological intercept method (Chayes, 1956; Rosiwal, 1898), provides the granulometric distribution.

To validate the method, we test various images and sedimentary deposits with different degrees of complexity. It was proved that under similar conditions, the accuracy obtainable by the OPTGRAN-CS program is within the range of variability of a manual count performed by experts. The method is robust, with easy-to-select parameters. Due to the high calculation speed, a larger number of particles can be analyzed accurately.

The possibility of performing automatic optical analysis of sedimentary deposits opens the possibility of new and important applications of optical granulometry methods, whose most important limitation was the long analysis times (Sarocchi et al., 2005, 2011). Furthermore the method is accessible to all, since it is based on digital photographs and free software.

2. Methods

In this section, the ECQMMF algorithm for segmenting and analyzing sedimentary images by means of stereological techniques is described, as well as its use in our specific application. Rosiwal's intercept method is also explained in more detail.

2.1. Entropy-Controlled Quadratic Markov Measure Field Models

The developed program is based on the segmentation methodology ECQMMF (Rivera and Dalmau, 2012) since this approach showed to be robust with respect to noise and hyperparameter initialization. The initial regions may be selected by the user and the resulting energy function is optimized iteratively. Moreover, hyperparameters related with the smoothing and the low entropy of the probability distribution of the regions to segment are easy to tune. Even more, the cost of this algorithm in terms of processing time is low because the function to optimize is quadratic with constant coefficients.

One of the characteristics of ECQMMF is its versatility, allowing segmentation based on different characteristics (Rivera and Mayorga, 2007; Rivera et al., 2007; Dalmau-Cedeno et al., 2007; Rivera et al., 2008; Rivera and Dalmau, 2012). In this work EC-QMMF has been used to perform multiclass segmentation. The model parameters are the mean and the covariance matrix of the RGB channels; these are calculated choosing a selected region of the image that will be named Model Parameters Sample Area. At the end of this process, different multiclasses are labeled in two categories, producing a binary image, where the background is labeled with zero and the foreground (selected clasts) with one. To this binary image (binary mask), it is successively applied the automatic Rosiwal intersects counting method.

Here follows a brief description of the EC-QMMF, as faithful as possible to Rivera and Dalmau (2012). First of all, it is necessary to select a region of interest for analyzing, where the scales and other unwanted objects do not appear in the scene. In Fig. 1, we show a region that we consider well selected and we will call simply image.

Let x be a pixel belonging to one of the M possible regions or classes, where $x \in \Omega = \{x_i i = 0,1, \ldots, N\}$and N is the number of pixels in the image. Denoting the set of classes as $M = \{M_c, M_A\}$, with $M_C = \{M_{c_1}, M_{c_2}, \ldots, M_{c_{n_1}}\}$and $M_A = \{M_{A_1}, M_{A_2}, \ldots, M_{A_{n_2}}\}$ where n_1 is the number of clasts models and n_2 the number of matrix models. Let's define the likelihood $v_k(x)$ as the probability of x belongs to a class k, such that $k \in M$ and $\sum_{k \in M} v_k(x) = 1$. Now, this likelihood may be defined as a multivariable normal probability distribution function given by

$$f(x|\mu_k, \Sigma_k) = \frac{1}{\sqrt{(2\pi)^3|\Sigma_k|}} exp\left(-\frac{1}{2}(x-\mu)^T\Sigma^{-1}(x-\mu)\right), \tag{1}$$

where $\mu_k \epsilon R^3$ and $\Sigma_k \epsilon R^3 \times R^3$are the mean and covariance matrix of this distribution, further, this statistics can be grouped in a parameter vector $\theta = \left\{((\mu_1, \Sigma_1), \ldots, (\mu_{n_1+n_2}, \Sigma_{n_1+n_2})\right\}$ and considering the pixel values $I(x)$ given by a parametric approach, we have

$$I(x) = \sum_{k=1}^{M} b_k(x)\phi(x; \theta_k) + n(x), \tag{2}$$

where $\phi(x;\theta_k)$ is the parametric model which defines its value, $n(x)$ is a independent random variables for each pixel x, and b_k is the indicator function region such that $\sum_{k=1}^{M} b_k(x) = 1, \ \forall \ x \in \Omega$. Using this model and assuming b as a MRF having a Gibbs distribution, one can reach to the following energy function;

$$\bigcup(b, \bar{\theta}) \approx \sum_{x \in \Omega} \sum_{k=1}^{M} b_k^2(x)\left[- log\ v_k(k) - \mu\right] + \lambda \sum_{\langle x,y \rangle} \|b(x) - b(y)\|^2. \tag{3}$$

The first term is related to the entropy likelihood whose typical values are $\mu \leq 0.5$; $\mu = 0.5$ is suggested in Rivera, et al. (2007). The

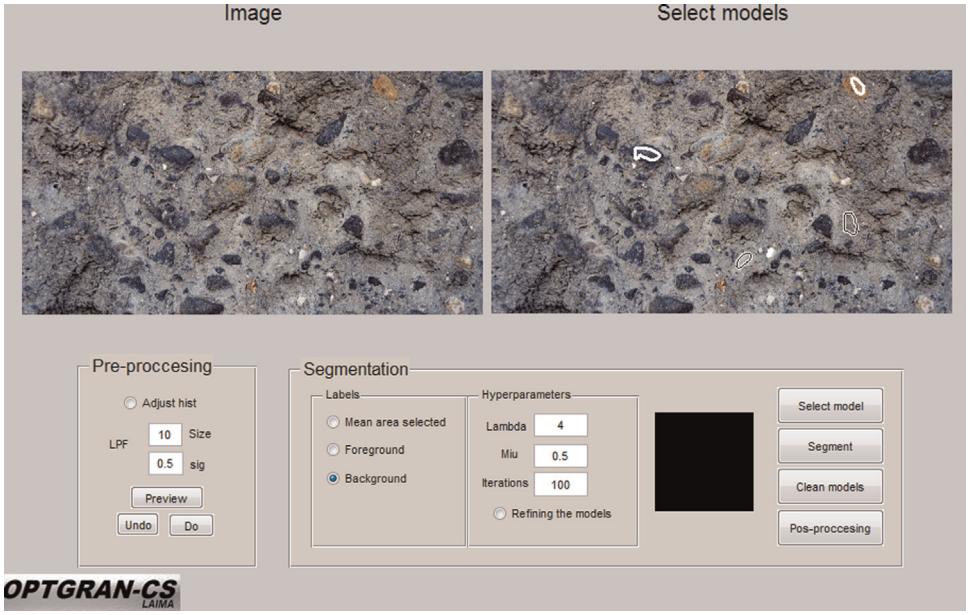

Fig. 1. Example of graphical user interface of the OPTRGRAN-CS software. The white lines in the right window enclose areas pertaining to different color models.

second term is related to the segmentation smoothness and spatial coherence; $\lambda = 4$ has been shown to give good results.

Finally, for our purposes, we need only two labels, one value for the foreground representing the clasts and the other (the background) for the matrix of the sedimentary deposit. So, the resulting binary image is defined as

$$\hat{I}(x) = \begin{cases} 1 & \forall\ x \in M_c \\ 0 & \forall\ x \in M_A \end{cases} \tag{4}$$

2.2. Rosiwal intercept method

Optical methods are based on stereology, a mathematical tool for efficient sampling, enabling reliable volumetric estimates with lower information processing (Mouton, 2002). Several reliable stereological methods exist (Sahagian and Proussevitch, 1998; Mouton, 2002; Sarocchi et al., 2005, 2011; Jutzeler et al., 2012). Starting with a digital photograph of the outcrop it is possible to relate the apparent granulometric areas (observed at the outcrop surface) with the true volumetric granulometry of the deposit.

The method applied here was proposed by Rosiwal (1898), and consists of measuring the intersections between particle outlines and an overlain array of lines (probes). This technique provides useful data to obtain the whole granulometric distribution (Sarocchi et al., 2005). Here we are using an arrangement such that the interline spacing of the probes must be set so that the largest clast in the image is not intercepted by more than two probe lines (Mouton, 2002; Sarocchi et al., 2005).

2.3. The OPTGRAN-CS software

The software developed here consists of three processing blocks. The first block is for image preprocessing. In this stage the software enables a region of interest to be chosen, enhances the contrast by color histogram equalization, and performs image smoothing by applying a lowpass filter. In a second block, segmentation is applied, and the user makes appropriate selections of the models of the clasts and matrix, the number of iterations and the value of the hyperparameters. The result of image segmentation is a binary image corresponding to the matrix and clast phases.

This block has a tool to reduce the noise of the binary mask, removing objects whose areas are below a set threshold. For very difficult cases where segmentation is not able to automatically separate clasts from the matrix, or when correctable differences can be detected with the naked eye, a simple manual editing can be performed. Finally, in the third block, Rosiwal's intercept counting method is applied. The main interface with its general features is shown in Fig. 1, and a full performance block diagram of the OPTGRAN-CS software is illustrated in Fig. 2.

2.4. Manual editing

The algorithm yields good results under certain conditions that will be analyzed in detail in the next sections. In some cases, there are images where automatic segmentation does not perform well because of the nature of the deposit. To solve these difficult cases

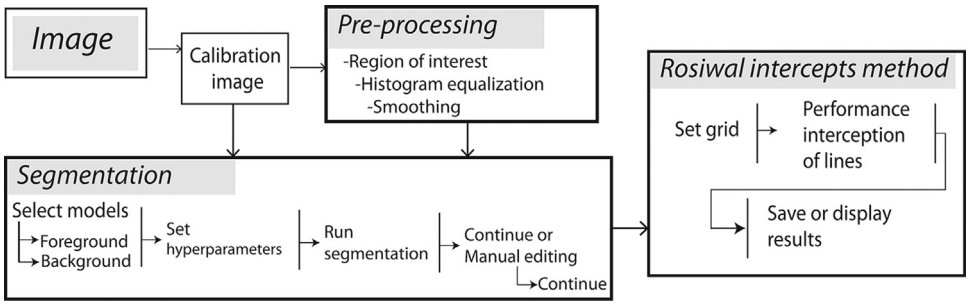

Fig. 2. Block diagram of the main three sections of the OPTRAGRAN-CS software.

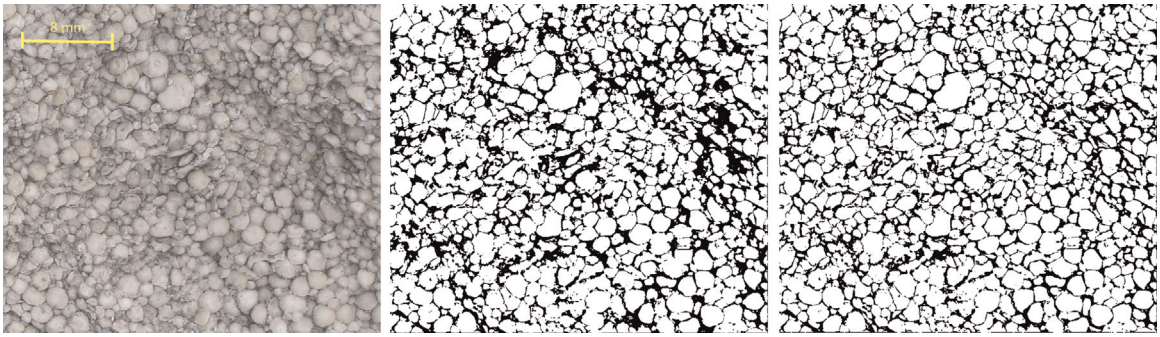

Fig. 3. Example of limestone where manual editing dramatically improves the results. The image in the center is automatically segmented. In the image at right, manual editing eliminates many of the contacts between clasts that cause errors in the analysis.

or to improve locally automatic segmented images, a software tool for manual editing was incorporated.

Fig. 3 shows a region of an image portraying an oolitic limestone deposit, very difficult to be segmented. This example demonstrates the utility of the manual editing step. It can be seen that automatic segmentation has generated errors; clasts of dark hues are taken as matrix. Moreover, in some cases, automatic segmentation finds contours that do not correspond to the real clast perimeters, and produces a sub-segmentation that causes two or more clasts to be recognized as one. These errors can be corrected manually. It is true that this requires further user intervention, but it still reduces the total time taken. In Fig. 4, the distributions obtained before and after the manual correction in two samples are shown.

We have presented imaging studies performed with particles between 2∅ (0.25 mm) and −7∅ (256 mm), but the method can operate at any scale. It can be usefully applied in other fields of science. The example in Fig. 5 shows the segmentation at a micron scale of an image of a sedimentary rock (argillaceous limestone) composed of a calcareous clay slurry and skeletal grain matrix. The distribution is used to determine the texture.

3. Results and discussion

The Rosiwal Intercept Method (M-RIM) applied manually, as shown in Sarocchi et al. (2005) and Sarocchi et al. (2016), provides granulometric data comparable with granulometric information obtained by sieving (discrepancy is on the order of 5–15%). Through a series of comparative studies (that can be consulted in the Supplementary material) where manual analysis was performed on the same set of images by four operators with different degrees of expertize, it could find that the average difference between measures is on the order of 10–15%. In this chapter the results of a series of studies that compare each other RIM and RIM applied automatically (A-RIM), is presented. They point out that the error associated with the automatic analysis is of the same order of magnitude or less than the error related with sieving and M-RIM.

3.1. Sedimentary deposits

Fifteen outcrops containing five different types of sedimentary deposits were analyzed. Table 1 summarizes some general geological characteristics of the deposits and gives some remarks about the performance of the OPTGRAN-CS process on segmentation of the images.

3.2. Comparison between methods on selected outcrops

The proposed automatic method (A-RIM) was compared to manual methods (M-RIM) performed by the experts on fifteen selected outcrops, each one differing in color, texture, clast shape and size, degree of clast overlapping, matrix vs. clast contrast, and other factors. The purpose of the comparison is to obtain a realistic panorama of sedimentary outcrop images where the A-RIM can be successfully applied and evaluate the discrepancy in accuracy with manual methods used to date.

The complete set of comparisons is reported in the Supplementary material. Here we examine three representative cases. Of these, two cases produced a very good approximation, and one gave results affected by errors.

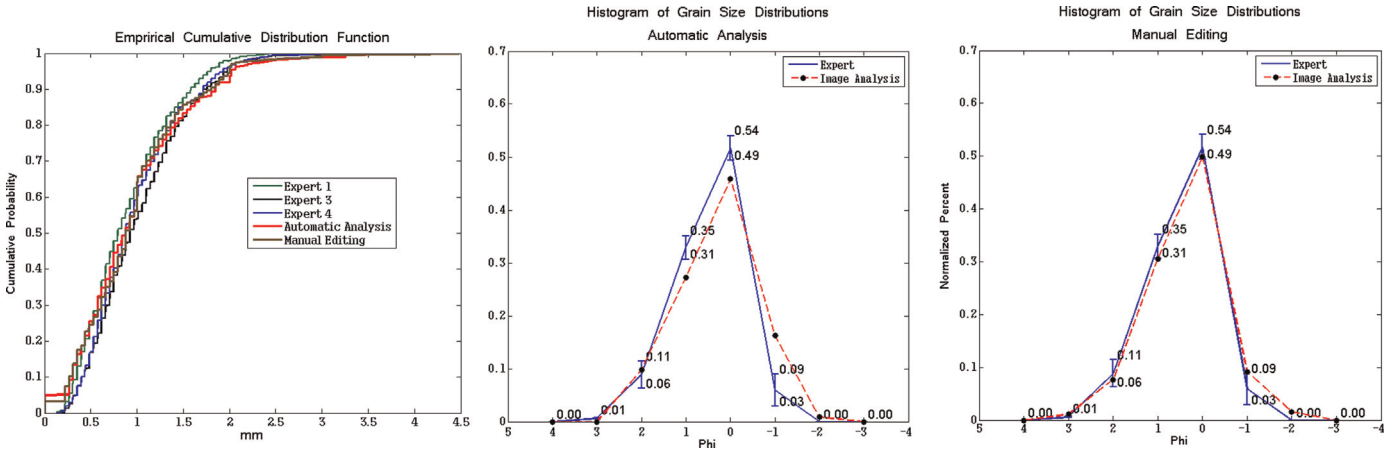

Fig. 4. Figure on the left represents the ECDF of different measurements of the same image. In the center the average grain size distribution obtained by human experts and by automatic analysis. At right, the average grain size distribution obtained by experts and automatic analysis after manual correction.

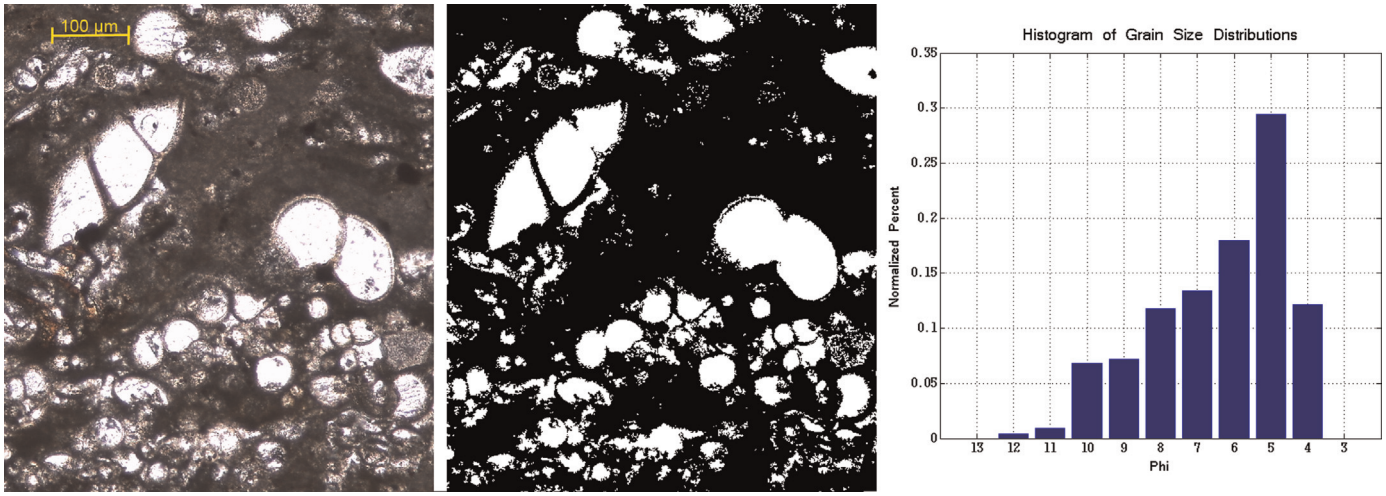

Fig. 5. The image is from the Eagle Ford Formation, taken with petrographic microscope foil; in the center the segmented image, and on the right the particle size distribution (73.7% matrix).

3.2.1. Mt. St. Helens pyroclastic density currents deposit (area 1.A)

The Mt. St. Helens PDC deposit produced by the May 18, 1980 eruption (Lipman, 1981; Brand et al., 2014), provides an excellent example of a deposit suitable for analysis with the program. The image of the outcrop, shown in Fig. 6, displays good contrast between clasts and matrix and few clasts that overlap or are tangent to each other. The hues of the clasts are few and the variance of the hues inside the clasts (color texture) is low.

Fig. 6 The area analyzed was 1.67 m^2 and the number of Rosiwal intercepts measured was about 1000. In order to evaluate the accuracy of the A-RIM method, first the manual analysis (see Fig. 6 and Table 2) of the best three experts were compared with each other, calculating the relative variance. The statistical parameters of the distribution were calculated using DECOLOG 5.1 software (Borselli and Sarocchi, 2004). It can be observed in Table 2 that all the distributions have almost the same statistical characteristics; means near 3.5 phi, poorly sorted, negatively skewed, and mesokurtic. The variance among the experts' M-RIM ranges from a maximum of $\pm 5\%$ to a minimum of $\pm 1\%$. The maximum discrepancy between the experts' mean M-RIM and A-RIM analysis is 2%. In addition, the statistical parameters are very similar, showing that with this kind of image the automatic method performs very well.

3.2.2. Irazú Rio Birris debris avalanche deposit (area 2.A)

Another analysis where good results were obtained is an outcrop of the Rio Birris debris avalanche deposits at Irazú Volcano (Pavanelli et al., 2004; Alvarado et al., 2006). The area analyzed was 0.06 m^2 and the number of Rosiwal intercepts measured was about 300. This image (Fig. 7) presents a good contrast between the clasts and matrix, and there is little overlap or joining of clasts. The analysis of this image is nevertheless somewhat more

Table 1
Description of the sedimentary deposits analyzed.

Location	Remarks
AREA 1: < Mt. St. Helens (MSH), Skamania County, Washington, United States. Pyroclastic deposit. See Fig. 4, Fig. A9*.	Active dacitic–andesitic stratovolcano. This deposit is one of the four primary pyroclastic density current units produced by the May 18, 1980 eruption (Brand et al., 2014). The images show a regular contrast between the clasts and matrix, overlapping of clasts is not present, and the hues of clasts and matrix tend to be homogeneous.
AREA 2: Irazu volcanic complex, Central Volcanic Cordillera, Costa Rica. Debris avalanche deposit. See Fig. 5, Fig. A4*.	Active andesitic–basaltic volcanic complex (Pavanelli et al., 2004; Alvarado et al., 2006). The deposit is a debris avalanche deposit that presents a good contrast between clasts and matrix. There is a little overlap or joining of clasts. Images are difficult to analyze due to different clast texture hues.
AREA 3: Joya Honda Maar, San Luis Potosí, Mexico. Pyroclastic deposit. See Fig. 6, Fig. A7*.	The Joya Honda Maar originated about 0.6 Ma from intraplate magmatism. This pyroclastic deposit was produced by a phreatomagmatic to magmatic eruption (Aranda-Gómez and Luhr, 1996). It shows a variety of clast and matrix types. The matrix has hues close to that of the clasts. The complexity of the textures makes the segmentation process more difficult.
AREA 4: Colima Volcano, Colima, Mexico. Epiclastic deposit. See Fig. A1, Fig. A2, and Fig. A3*.	Active volcano that has had explosions, collapses, lava flow, and dome detachments in the last six years (Saucedo et al., 2002, Sarocchi et al., 2011). The images of the pyroclastic deposit are characterized by good contrast between clasts and matrix, but there is considerable overlap between clasts, which in some cases causes errors in the segmentation.
AREA 5: Nevado de Toluca Volcano, Toluca, Mexico. Debris avalanche deposit. See Fig. A5 and Fig. A6*.	Andesitic–dacitic stratovolcano with domes and collapsed sectors (Capra et al., 2008). The outcrop is from a debris avalanche deposit. One feature that impedes efficient segmentation is that the matrix has several different colors. For this reason it is likely that matrix models are similar to that of some of the clasts.
AREA 6: Dawlish Bay, Devon, United Kingdom. Sedimentary breccia. See Fig. A10*.	Holocene polygenic sedimentary breccia. The image is characterized by clasts of different colors but the matrix color is very homogeneous. Clasts barely overlap. The image is easy to analyze.
AREA 7: Limestone nodulosa-Teba, Málaga, Spain. Sedimentary deposit. See Fig. A11*.	The image of sedimentary limestone shows homogeneous hues. In spite of low contrast between matrix and clasts and the edges of the clasts not being well defined, the program allows segmentation. Good performance.
AREA 8: Sierra de Grazalema, Spain. Colluvium deposit. See Fig. A8*.	Colluvium deposits with soil formation in the upper part. The image has very contrasted features (matrix and clasts) that enable good segmentation.

* These figures are available at supplementary material.

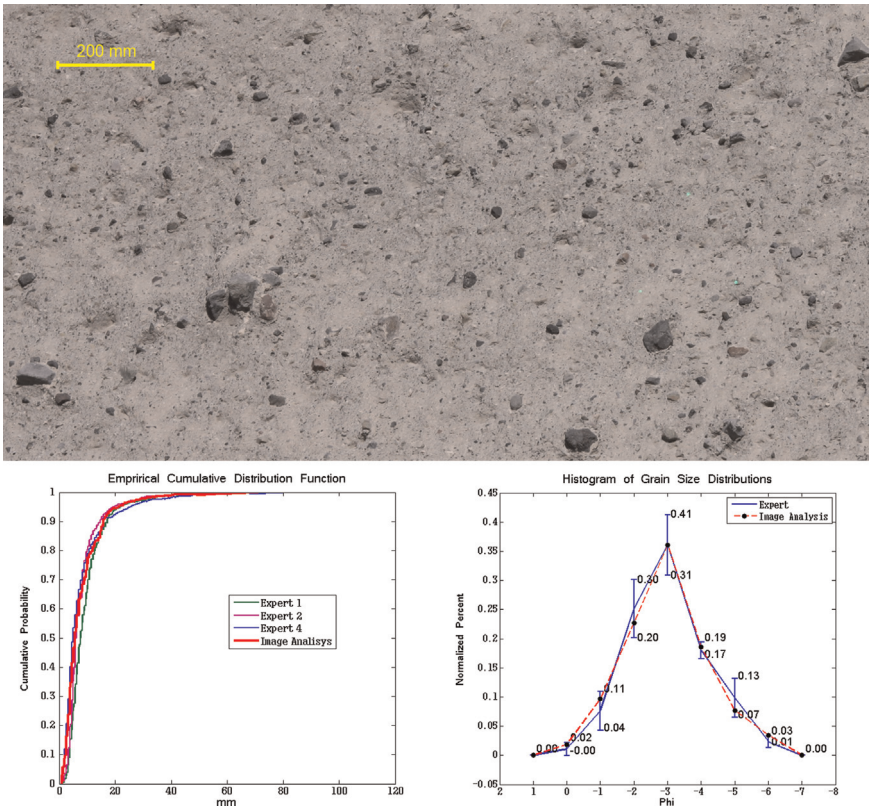

Fig. 6. Outcrop of Mt. St. Helens PDC deposit, Area 1.A. In the lower left graph, the ECDF curve of M-RIM obtained by the best three experts and the A-RIM results are shown. In the bottom right graph, the mean and variance of the experts' M-RIM measures (solid line) is compared with the curve obtained by A-RIM (dotted line). The almost perfect fit demonstrates the good performance of A-RIM on similar images.

Table 2
Statistical parameters of particle size distributions obtained by interpolating the cumulative distribution function DECOLOG 5.1.

Measure	Mean ∅	Standard deviation ∅	Skewness ∅	Kurtosis ∅
M-RIM Expert 1	−3.8	1.10	−0.23	0.94
M-RIM Expert 2	−3.4	1.02	−0.17	1.11
M-RIM Expert 4	−3.6	1.01	−0.44	1.04
M-RIM Expert mean	−3.6	1.04	−0.28	1.03
A-RIM	−3.4	1.21	−0.06	1.10

complicated than the previous one because the clasts have different hue textures. It can be observed (Fig. 7) that most clasts are dark, but have some light colored texture inside, similar to the matrix. This can be resolved with binary image processing as long as the treated areas are convex sets. The result of the analysis by the automatic method is within the variability of manual counting, which has a maximum difference of ±5% and a minimum of ±1.5%, and ECDF tends to have the same range. The maximum difference between mean M-RIM and A-RIM analysis is 2%.

3.2.3. *Joya Honda maar, pyroclastic density currents deposit (area 3. A)*

The image of a pyroclastic density current deposit at Joya Honda maar (Aranda-Gómez and Luhr, 1996; Aguillón-Robles et al., 2014), shown in Fig. 8, is an example where the A-RIM method found some problems and the error introduced by the automatic analysis is outside the range of variability from manual counting. The area analyzed was 2.16 m^2 and the number of Rosiwal intercepts measured was about 250. The variance among the experts ranged from a maximum of ±10% to a minimum of 2%. The maximum discrepancy between the experts' mean M-RIM and A-RIM analysis was 13%. The difference between the M-RIM and A-RIM methods is considerable because the image has a great variety of clast models. The matrix has a hue very close to that of the clasts, making matrix texture segmentation difficult. The granulometric distribution histogram shows the largest differences of the three example cases, especially in granulometric classes 0∅ (1–2 mm) and −4∅ (16–32 mm). A possible explanation for this poor performance is that fine particles can be confused with clast texture and the program may erroneously consider a set of them as a larger clast. This could explain the higher abundance of larger clasts found by the program. Although the A-RIM count falls outside the variability of M-RIM manual counting, the error can still be considered as tolerable for some geological studies.

3.3. *Influence of optical resolution on measurement accuracy*

Camera resolution is important for obtaining accurate optical granulometric measurements. Three cameras with different optics are tested to demonstrate the influence of resolution on data accuracy: (A) a professional DSLR, Canon EOS 50D camera with 15 megapixels (Mp) resolution, (B) a tablet iPad 4 A1458 camera with 5 Mp, and (C) a mobile phone Samsung Galaxy S3 mini camera with 3.2 Mp resolution. Photographs were taken of the same area (0.16 m^2), from the same distance (1 m) and at the same time (sequentially). The resolution for each camera is reported in Table 3. Differences in resolution between cameras is demonstrated visually in Fig. 9.

Fig. 9 The general shape of the granulometric distribution and size of the largest clasts present in the analyzed field are the same between the cameras (graphs in Fig. 9). The primary difference is a

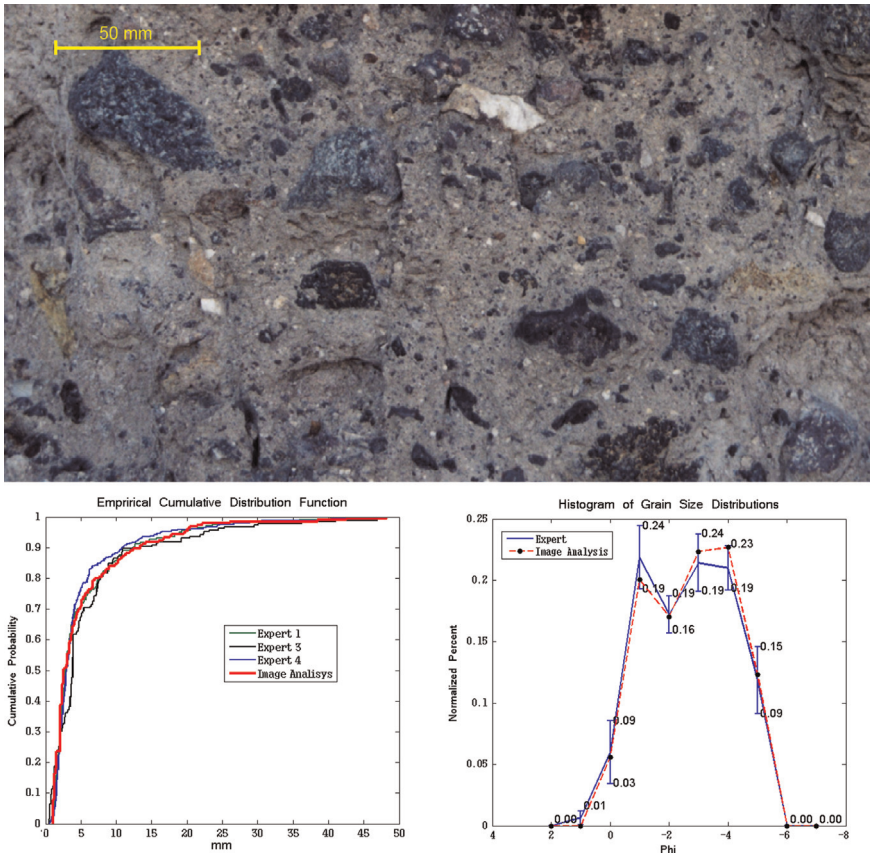

Fig. 7. Results of manual measurement and automatic method in an area of the Irazú Volcano. The lower left graph shows the ECDF and the lower right graph shows the phi distribution scale.

shift of the modal class toward finer-grained with the high resolution camera, which is missed when using a low resolution camera. Given this result, the smallest observable clast for a 15 Mp DSLR camera is ~300 μm, with an iPad tablet camera is up to ~1 mm, and with a Smartphone (3.2 Mp) camera is ~3 mm. In addition, a qualitative comparison established that a clast to be considered real (not noise) must consist of at least 12 pixels. Thus, while the best option to perform an optical particle size analysis is a camera with high resolution and a metric flat field objective, a simple low cost smartphone camera, at the distance of 1 m, allows clast measurements above ~2 mm and produces similar results as those from sieving. However, since lower optical quality can deform the image edges, performing the analysis using only the central portion of the field is recommended.

3.4. General discussion of the A-RIM method

The OPTGRAN-CS software provides added value to optical granulometric methods, whose most evident limit was the need to make measurements semi-manually (Sarocchi et al., 2005, 2016). The software based on the ECQMMF segmentation algorithm using color segmentation enables phases with very similar tones to be segmented quickly and accurately. The software is freeware, and the user-friendly graphical interface makes it easy to use. The software has functions that enable simple, accurate calibration, a basic esthetic image processing module, and a manual editing routine that allows it to be used on virtually any type of image. The software can be used with any capture device, but the higher the resolution the higher the accuracy that can be achieved. While high resolution and flat field objective lenses allow precise analysis of the whole granulometric distribution, a simple, low-cost

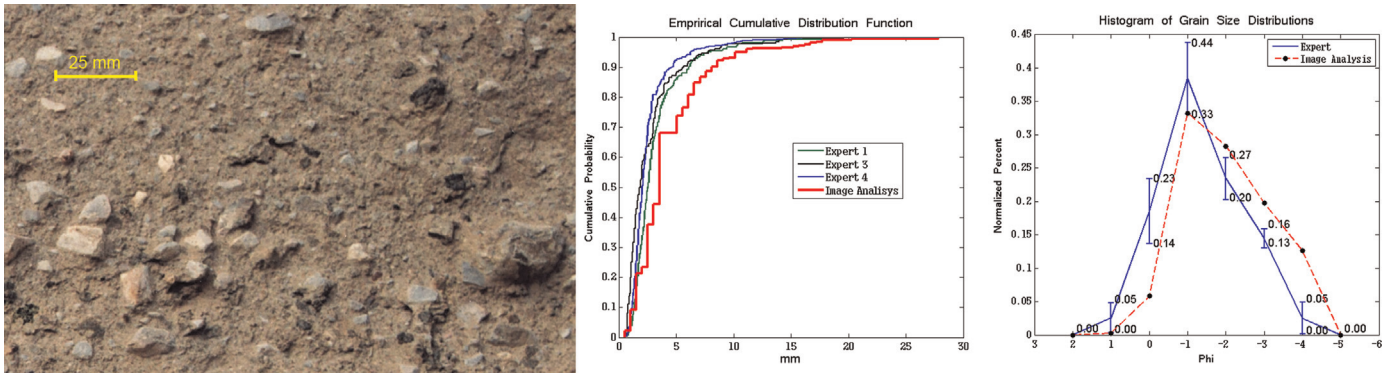

Fig. 8. Sedimentary deposit of Joya Honda Maar. The center graph shows the ECDFs and the right graph compares the distributions of the two methods.

Table 3
Optical characteristics of cameras.

Camera	Technical notes	Pixel size	Size of finest measurable clast
DSLR Canon D50	15 Mp camera, obj. zoom 28–70 mm focal length, used at 50 mm f.l. No distortion is observed in the visual field.	0.15 mm/px	~0.3 mm
Tablet iPad 4 A1458	5 Mp camera, serial objective. No appreciable distortion is observed in the visual field.	0.25 mm/px	~1 mm
Samsung Galaxy S3 mini	3.5 Mp camera, 4× optical zoom. No appreciable distortion is observed in the visual field.	0.98 mm/px	~3 mm

smartphone camera can also provide useful analysis of the coarser (>2 mm) components. The comparison with the Rosiwal intercept method applied semi-manually shows generally good agreement. 90% of the comparative analysis had a maximum difference less than 10% from granulometric data obtained by A-RIM or was within the variance of manual measures performed by expert human operators (see Table 4 and Supplementary material).

This result can be considered a great success, considering that the analyses were done in comparable conditions. On the other hand, the supervised automatic program performs the analysis five to ten times faster. This means that a greater number of particles can be analyzed in less time, enabling the analysis of greater areas with a significant increase in accuracy.

Like any automated program, there are limits in the program's ability to distinguish the clasts, which differ in characteristics not considered by the algorithm, such as texture and shape. Furthermore, factors such as the characteristics of the scene, illumination, presence of shadows, clasts in contact with each other, water stains or vegetation, similar texture and colors in clasts and matrix can alter the measurements.

4. Conclusions

The program proposed here, based on the ECQMMF algorithm, carries out image segmentation by means of a sophisticated analysis of colors, and enables optical granulometric analysis to be performed quickly and accurately. The method greatly reduces analysis time by allowing studies of larger areas in a short time, giving a better basis for interpretation of sedimentary deposits. The new method was tested on a large variety of different sedimentary deposits originating in very different sedimentological environments.

The comparison made between the M-RIM and A-RIM shows that with parity of conditions, granulometry provided by the supervised automatic analysis falls within the range of variability obtained by semi-manual measurements made by experts for images with good contrast between the matrix and clasts. In the worst conditions, the discrepancy between the automatic and semi-manual method is less than 13%, a discrepancy that is very close to the natural internal variability of coarse sedimentary deposits, and thus tolerable for many sedimentological studies. Moreover, this discrepancy can be notably reduced increasing the number of intercepts or by manual editing.

The new method can be used not only in sedimentology and

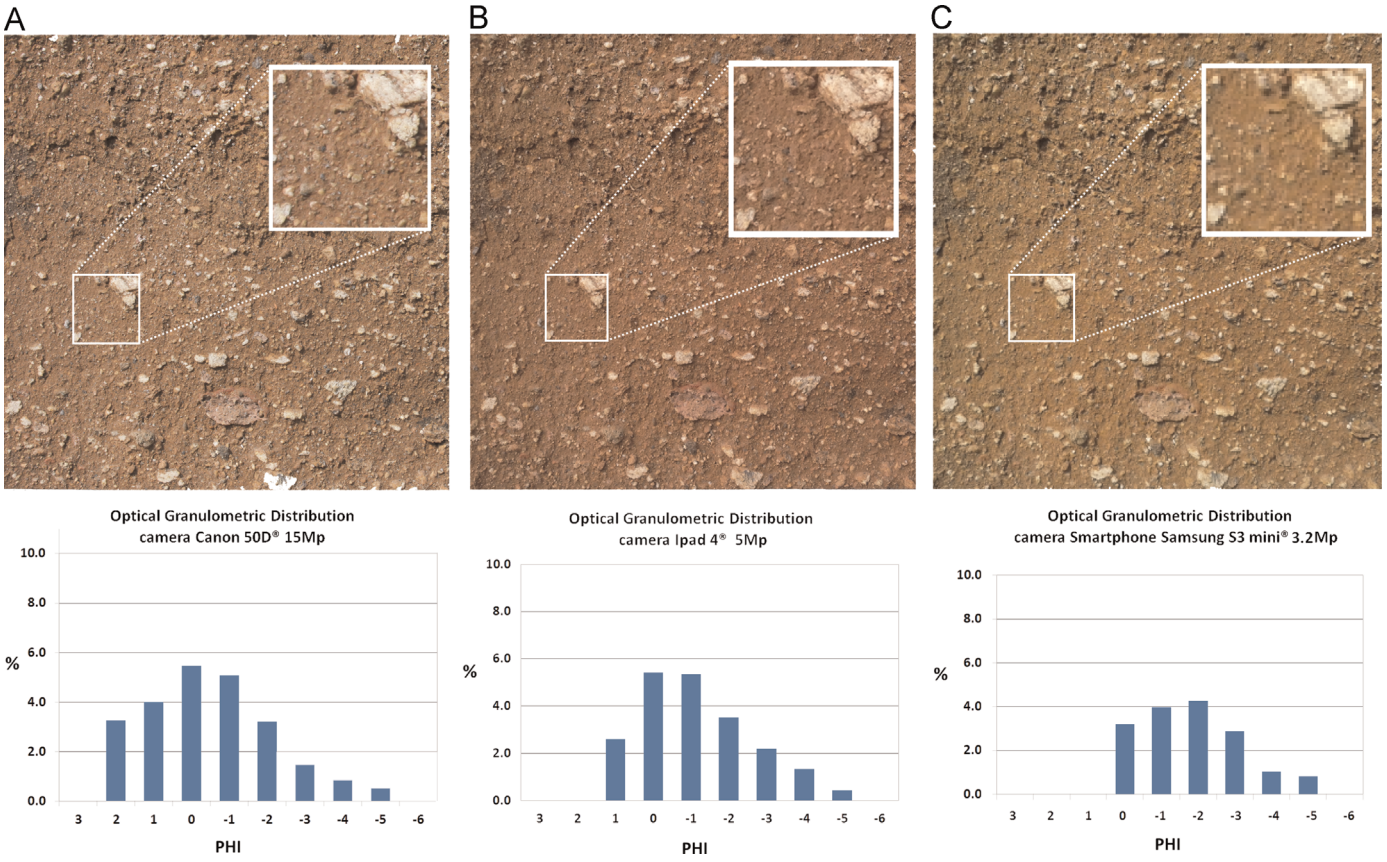

Fig. 9. Comparison of the image quality and optical granulometry distributions, obtained using cameras with different resolution on the same area test of a pyroclastic deposit (ignimbrite). (A) Images of 15 Mp, (B) 5 Mp, (C) and 3.2 Mp resolution.

Table 4
Summary of the results of the analysis of the 14 statistical parameters obtained with DECOLOG 5.1.

Outcrop	Area m^2	Intersections	Mean M-RIM /A_RIM	Sorting M-RIM /A_RIM	Skewness M-RIM /A_RIM	Max. difference M-RIM and A_RIM	Analysis time M-RIM /A_RIM (min)*
Area 1.A	1.67	1000	−3.50/−3.40	1.21/1.13	−0.12/−0.06	2%	>60/<7
Area 1.B	0.45	500	−3.18/−3.07	1.10/1.34	0.03/0.07	5%	>45/<5
Area 2.A	0.07	300	−3.17/−3.25	1.45/1.43	0.05/0.10	2%	>35/<5
Area 2.B	0.15	350	−3.33/−3.34	1.50/1.55	−0.01/0.2	6%	>40/<5
Area 3.A	2.16	250	−1.76/−2.56	1.06/0.95	−0.19/−0.20	13%	>30/<5
Area 3.B	0.08	150	−4.36/−4.52	0.99/1.11	0.16/0.27	5%	>25/<3
Area 4.A	2.26	400	−5.32/−522	1.12/1.05	−0.02/0.17	4%	>40/<5
Area 4.B	0.48	110	−5.13/−5.01	0.88/1.05	0.19/0.19	4%	>25/<3
Area 4.C	0.08	500	−2.84/−2.75	1.11/1.11	0.09/0.25	5%	>50/<5
Area 5.A	0.08	400	−2.87/−2.82	1.03/1.12	0.01/−0.17	7%	>40/<5
Area 5.B	0.05	150	−2.46/−2.23	1.06/1.30	−0.02/0.04	8%	>25/<3
Area 6.A	0.64	400	−4.47/−4.39	0.97/1.13	−0.12/−.01	6%	>45/<5
Area 7.A	0.18	370	−4.65/−.4.32	1.37/1.60	−0.01/−0.04	9%	>30/<5
Area 8.A	1.14	300	−5.32/−5.14	1.43/1.56	0.10/0.13	4%	>30/<3

* Time to perform A-RIM includes these steps: pre-processing, segmentation, morphological binary operation and the count by Rosiwal intercepts. ECQMMF segmentation was performed with 100 iterations.

earth science but also extended to other disciplines. It can be easily employed by the scientific community at no cost. The full software package, under a freeware license, can be downloaded at http://www.laima-uaslp.org/descargas.html. The software will be continuously updated, and a new editing function, image processing procedure and new algorithms using different segmentation criteria are being developed and will be available soon.

Acknowledgments

We wish to thank Luis Angel Rodríguez Sedano, Ilze Sanchez Marin and Luis Felipe Rodriguez Quibrera for their help during the experimental work. We are also grateful to Margaret Schroeder Urrutia and Brittany Brand for refine the English version of the paper.

This work was partially supported by Ciencias Básica CONACyT projects (SEP-83301) and CONACYT- Ciencia Básica-2012-01 – 184060, PROMEP UASLP-PTC-241, Instituto Panamericano de Geografía e Historia. H Gamaliel Moreno Chávez acknowledges CONACYT for the PhD grant (No. 229958).

Appendix A. Supplementary material

Supplementary data associated with this article can be found in the online version at http://dx.doi.org/10.1016/j.cageo.2015.09.007.

References

Aguillón-Robles, A., Tristán-González, M., Aguirre-Díaz, G. de Jesús, López-Doncel, R.A., Bellon, H., Martínez-Esparza, G., 2014. Eocene to quaternary mafic-intermediate volcanism in San Luis Potosí, central Mexico: the transition from Farallon plate subduction to intra-plate continental magmatism. J. Volcanol. Geotherm. Res. 276, 152–172.

Alvarado, G.E., Carr, M.J., Turrin, B.D., Swisher, C.C., Schmincke, H.-U., Hudnut, K.W., 2006. Recent volcanic history of Irazú volcano, Costa Rica: alternation and mixing of two magma batches, and pervasive mixing. Geol. Soc. Am. Spec. Pap. 412, 259–276.

Allen, J.R.L., 1997. Subfossil mammalian tracks (Flandrian) in the severn estuary, s. w. Britain: mechanics of formation, preservation and distribution. Philos. Trans. R. Soc. B: Biol. Sci. 352, 481–518.

Aranda-Gómez, J., Luhr, J.F., 1996. Origin of the Joya Honda maar, San Luis Potosí, México. J. Volcanol. Geotherm. Res. 74, 1–18.

Beuselinck, L., Govers, G., Poesen, J., Degraer, G., Froyen, L., 1998. Grain-size analysis by laser diffractometry: comparison with the sieve-pipette method. CATENA 32, 193–208.

Borselli, L., Sarocchi, D., 2004. Deconvolution of Mixture's Components Inside Particle Size Distributions (DECOLOG) [Online]. Available: ⟨http://www.decolog.org/⟩ (Accessed September 2014).

Boudon, G., Camus, G., Gourgaud, A., Lajoie, J., 1993. The 1984 nuée-ardente deposits of Merapi volcano, Central Java, Indonesia: stratigraphy, textural characteristics, and transport mechanisms. Bull. Volcanol. 55, 327–342.

Brand, B.D., Mackaman-Lofland, C., Pollock, N.M., Bendaña, S., Dawson, B., Wichgers, P., 2014. Dynamics of pyroclastic density currents: conditions that promote substrate erosion and self-channelization—Mount St Helens, Washington (USA). J. Volcanol. Geotherm. Res. 276, 189–214.

Capaccioni, B., Sarocchi, D., 1996. Computer-assisted image analysis on clast shape fabric from the Orvieto-Bagnoregio ignimbrite (Vulsini District, central Italy): implications on the emplacement mechanisms. J. Volcanol. Geotherm. Res. 70, 75–90.

Capaccioni, B., Valentini, L., Rocchi, M.B.L., Nappi, G., Sarocchi, D., 1997. Image analysis and circular statistics for shape-fabric analysis: applications to lithified ignimbrites. Bull. Volcanol. 58, 501–514.

Capra, L., Norini, G., Groppelli, G., Macías, J.L., Arce, J.L., 2008. Volcanic hazard zonation of the Nevado de Toluca volcano. J. Volcanol. Geotherm. Res. 176, 469–484.

Chayes, F., 1956. Petrographic Modal Analysis. John Wiley, New York.

Chermant, J.-L., 2001. Why automatic image analysis? An introduction to this issue. Cem. Concr. Compos. 23, 127–131.

Dalmau-Cedeno, O., Rivera, M., Mayorga, P.P., 2007. Computing the α-channel with probabilistic segmentation for image colorization. Computer Vision, 2007. ICCV 2007. In: Proceedings of IEEE 11th International Conference on, 14–21 October 2007. pp. 1–7.

Fernlund, J.M.R., 1998. The effect of particle form on sieve analysis: a test by image analysis. Eng. Geol. 50, 111–124.

Folk, R.L., 1966. A review of grain-size parameters: sedimentology. Sedimentology 6, 73–93.

Freundt, A., Schmincke, H.U., 1986. Emplacement of small-volume pyroclastic flows at Laacher See (East-Eifel, Germany). Bull. Volcanol. 48, 39–59.

Gee, G.W., Bauder, J.W., 1986. Particle-size analysis1. In: KLUTE, A. (Ed.), Methods of Soil Analysis: Part 1—Physical and Mineralogical Methods. Soil Science Society of America, American Society of Agronomy, Madison.

Glenn, S.V., 1969. Grain size distributions and depositional processes. J. Sediment. Petrol. 39 (3), 1074–1106.

Jutzeler, M., Proussevitch, A.A., Allen, S.R., 2012. Grain-size distribution of volcaniclastic rocks 1: a new technique based on functional stereology. J. Volcanol. Geotherm. Res. 239–240, 1–11.

Kaye, B.H., Alliet, D., Switzer, L., Turbitt-Daoust, C., 1999. Effect of shape on intermethod correlation of techniques for characterizing the size distribution of powder. Part 2: Correlating the size distribution as measured by diffractometer methods, TSI-Amherst aerosol spectrometer, and Coulter Counter. Part. Part. Syst. Charact. 16, 266–272.

Konert, M., Vandenberghe, J.E.F., 1997. Comparison of laser grain size analysis with pipette and sieve analysis: a solution for the underestimation of the clay fraction. Sedimentology 44, 523–535.

Lajoie, J., Boudon, G., Bourdier, J.L., 1989. Depositional mechanics of the 1902 pyroclastic nuéeardente deposits of Mt. Pelée, Martinique. J. Volcanol. Geotherm. Res. 38, 131–142.

Lewis, D., Mcconchie, D., 1994. Analytical Sedimentology, 1st ed. Chapman & Hall, New York.

Lipman, P.W., Mullineaux, D.R., 1981. The 1980 eruptions of Mount St. Helens, Washington. US Geological Survey Professional Paper, Washington, DC, United States, p. 1250.

Lirer, L., Vinci, A., 1991. Grain-size distributions of pyroclastic deposits. Sedimentology 38, 1075–1083.

Loizeau, J.L., Arbouille, D., Santiago, S., Vernet, J.P., 1994. Evaluation of a wide range laser diffraction grain size analyser for use with sediments. Sedimentology 41, 353–361.

Lovell, C.J., Rose, C.W., 1991. Wake-capture effects observed in a comparison of methods to measure particle settling velocity beyond stokes' range. J. Sediment. Petrol. 61 (4), 575–582.
Moreno Chávez, G., Sarocchi, D., Arce Santana, E., Borselli, L., Rodríguez-Sedano, L. A., 2014. Using Kinect to analyze pebble to block-sized clasts in sedimentology. Comput. Geosci. 72, 18–32.
Mouton, P., 2002. Principles and Practices of Unbiased Stereology: An Introduction for Bioscientists. The Johns Hopkins University Press, Baltimore and London.
Nichols, G., 2009. Sedimentology and Stratigraphy. John Wiley & Sons, United States.
Olgun, E., Norman, T., 1993. Grain size analysis of some olistostrome between Balkuyumcu and Alci, (SW of Ancara). Bull. Miner. Res. Explor. 115, 31–48.
Pavanelli, N., Capaccioni, B., Sarocchi, D., Calderoni, G., Vaselli, O., Tassi, F., Duarte, E., 2004. Geology and stability of the southern flank of Irazu volcano, Costa Rica. Acta Vulcanol. 16 (1), 1–7.
Pettijohn, F.J., 1987. Sand and Sandstone. Springer Science & Business Media, United States of America.
Rivera, M., Dalmau, O., 2012. Variational Viewpoint of the Quadratic Markov Measure Field Models: Theory and Algorithms. Image Process., IEEE Trans. 21, 1246–1257.
Rivera, M., Dalmau, O., Tago, J., 2008. Image segmentation by convex quadratic programming. In: Proceedings of the Pattern Recognition, 2008. ICPR 2008. 19th International Conference on, 8–11 December 2008. pp. 1–5.
Rivera, M., Mayorga, P.P., 2007. Quadratic Markovian probability fields for image binary segmentation. Computer Vision, 2007. ICCV 2007. In: Proceedings of IEEE 11th International Conference on, 14–21 October 2007. pp. 1–8.
Rivera, M., Ocegueda, O., Marroquin, J.L., 2007. Entropy-Controlled Quadratic Markov Measure Field Models for efficient image segmentation. Image Process., IEEE Trans. 16, 3047–3057.
Rosiwal, A., 1898. Über geometrische Gesteins-analysen. Ein facher Weg zur zifermässigen Feststellung des Quantitätsverhältnisses der Mineral bestandteile gemengter Gesteine. Verh. Königlich-Kaiserliches Geol. Reichsamt (Wien), 143.
Rubin, D.M., 2004. A simple autocorrelation algorithm for determining grain size from digital images of sediment. J. Sediment. Res. 74, 160–165.
Sahagian, D.L., Proussevitch, A.A., 1998. 3D particle size distributions from 2D observations: stereology for natural applications. J. Volcanol. Geotherm. Res. 84, 173–196.
Sarocchi, D., Borselli, L., Macías, J.L., 2005. Construcción de perfiles granulométricos de depósitos piroclásticos por métodos ópticos. Rev. Mex. Cienc. Geol. 22, 371–382.
Sarocchi, D., Borselli, L., Rodriguez-Sedano, L.A., Moreno Chávez, G., Brand, B.D., 2016. Laser Remote Optical Granulometry: a method to obtain granulometric analysis of inaccessible or compacted sedimentary deposits from distance. J. Volcanol. Geotherm. Res.
Sarocchi, D., Sulpizio, R., Macías, J.L., Saucedo, R., 2011. The 17 July 1999 block-and-ash flow (BAF) at Colima Volcano: new insights on volcanic granular flows from textural analysis. J. Volcanol. Geotherm. Res. 204, 40–56.
Saucedo, R., Macias, J.L., Bursik, M.I., Mora, J.C., Gavilanes, J.C., Cortes, A., 2002. Emplacement of pyroclastic flows during the 1998–1999 eruption of Volcán de Colima, México. J. Volcanol. Geotherm. Res. 117, 129–153.
Saucedo, R., Macías, J.L., Sarocchi, D., Bursik, M., Rupp, B., 2008. The rain-triggered Atenquique volcaniclastic debris flow of October 16, 1955 at Nevado de Colima Volcano, Mexico. J. Volcanol. Geotherm. Res. 173, 69–83.
Valsangkar, A.J., 1992. Principles, Methods and Applications of Particle Size Analysis. NRC Research Press.
Walker, G.P.L., 1971. Grain-Size Characteristics of Pyroclastic Deposits. J. Geol. 79 (6), 696–714.
Yamazaki, T., Kato, I., Muroi, I., Abe, M., 1973. Textural analysis and flow mechanism of the Donzurubo subaqueous pyroclastic flow deposits. Bull. Volcanol. 37, 231–244.